Fast Quantitative Microwave Imaging With Scattered-Power Maps

Denys S. Shumakov, *Graduate Student Member, IEEE*, and Natalia K. Nikolova, *Fellow, IEEE*

Abstract—A new direct-inversion method, scattered-power mapping (SPM), for fast quantitative microwave imaging is introduced. It builds on a recently proposed inversion strategy that demonstrated quantitative direct reconstruction with experimentally acquired system point-spread functions. In comparison with this initial work, SPM features a drastic improvement in the computational time along with reduced number of calibration measurements. Moreover, SPM is versatile allowing a forward model of scattering cast either as a linearized Born model or as a Rytov model. SPM is intended as a tool to solve weak-scattering problems or as a linear-inversion module within nonlinear iterative reconstruction.

Index Terms—Born approximation, direct inversion, linear inversion, microwave imaging, Rytov approximation.

I. INTRODUCTION

FOR decades, near-field microwave imaging methods have been developed for applications in nondestructive testing and evaluation, underground surveillance, through-the-wall imaging, concealed weapon detection, and biomedical diagnostics [1]–[7], in particular for early stage breast cancer diagnostics [8], [9]. The relatively cheap and compact apparatus, the nonionizing radiation, and the relatively good penetration make microwaves appealing in imaging.

Real-time microwave imaging techniques usually offer only qualitative reconstruction. They are based on the linearized model of scattering allowing for quick inversion. However, the outcome may not be satisfactory due to the approximations used in the linearization. Holographic [10]–[12], time-reversal [13], [14], sensitivity-based [15], [16], and confocal [17], [18] methods belong to the category of qualitative methods.

The quantitative reconstruction of the dielectric profile usually requires solving the nonlinear scattering problem. Theoretically, this intrinsically ill-posed problem can take into account multiple-scattering effects and is valid for scatterers of any electrical size and dielectric contrast. It is tackled by using time-consuming iterative approaches (often with

the proper regularization strategy), the convergence of which critically depends on the fidelity of the forward model. Born iterative methods [19]–[21] and model-based optimization methods [9], [22], [23] are the most common quantitative techniques in microwave near-field imaging.

In [24] and [25], an approach to linear yet quantitative imaging has been proposed. The key lies in the experimentally acquired resolvent kernel, which properly scales the inversion problem thereby enabling quantitative imaging. The kernel is acquired with a measurement of a calibration object (CO). Here, we propose a new method, scattered-power mapping (SPM), which exploits the key idea of the work in [24], but is more general and far more efficient in solving the linear inverse problem.

The first important improvement offered by the SPM is that it can employ the Rytov approximation, in addition to also being capable of employing the linear Born model of scattering. The Rytov approximation is subject to a different set of limitations compared to the Born approximation; therefore, the applicability of the method is significantly expanded.

Second, a new method of building the SPM system matrix is proposed although its physical meaning of being the image point-spread function (PSF) remains the same as initially introduced in [24]. The new method has two advantages: 1) significantly reduced system-calibration effort and 2) the running time is two orders of magnitude less than that in [24]. For the case of planar acquisition surfaces and when the background is homogeneous or layered (translationally invariant systems), it is no longer required to have a four-times larger scanning area for the CO measurement as it was in [24] and [25]. The use of a coordinate translation in k-space leads to the system matrix being block circulant with circulant blocks (BCCB) in the case of 2-D imaging or block circulant with BCCB blocks in 3-D imaging. It is well known that circulant matrices can be diagonalized by a discrete Fourier transform. Hence, the respective linear equations can be quickly solved using the fast Fourier transform (FFT) [26], [27].

Third, with wideband data, an improved normalization of the power maps at all frequencies is developed. This normalization allows for combining all frequency samples into a single power map, which is then processed by the SPM. In this way, the stronger signals at lower frequencies have the same impact on the overall result as the weaker signals at higher frequencies. This feature is essential for maintaining good penetration without sacrificing image resolution. Moreover, the same normalization strategy can be applied to combine reflection and transmission data of different magnitudes.

II. SPM Theory

A. Forward Model Formulation

The reconstruction theory presented here is cast in the frequency domain, however, it can accommodate time-domain measurements as well. Note that all frequency-domain quantities incorporate the $\exp(i\omega t)$ time-harmonic factor, where $i = \sqrt{-1}$, ω is angular frequency, and t is time.

In frequency-swept measurements, a network of N_r receivers (Rxs) and N_t transmitters (Txs) acquires the data at N_f frequencies $f^{(m)}$ ($m = 1, \ldots, N_f$), one frequency at a time. Here, we assume that the data are in the form of S-parameters $S_{ij}^{(m)}$ ($i = 1, \ldots, N_r$ and $j = 1, \ldots, N_t$). This is why the scattering model presented next is cast in terms of the S-parameters.

In microwave imaging, it is beneficial to deal with a data equation where the data are the actual responses, not the **E**-field as in [24]. Since the measured responses in our case are S-parameters, the data equation is stated accordingly (see [29])

$$S_{\text{OBJ},n}^{(m)}(\mathbf{r}) = S_{\text{RO},n}^{(m)}(\mathbf{r}) + \kappa_n^{(m)} \int_{V'} \Delta\varepsilon_{\text{OBJ}}(\mathbf{r}')$$
$$\times \left[\mathbf{E}_{\text{RO},i}^{(m)}(\mathbf{r}'; \mathbf{r}) \cdot \mathbf{E}_{\text{OBJ},j}^{(m)}(\mathbf{r}'; \mathbf{r}) \right] d\mathbf{r}' \quad (1)$$

where $n = 1, \ldots, N_t \cdot N_r$ is the response index, $m = 1, \ldots, N_f$ is the frequency sample index, $\mathbf{r}'$ is the position inside the inspected volume V', whereas $\mathbf{r}$ is the observation position. Each nth experiment corresponds to a unique (ij) antenna pair, where the position of the ith (Rx) antenna is given by $\mathbf{r}$. Throughout this paper, position vectors and vectors of physical fields are in upright bold, whereas matrices are in italic bold. The complex constant at the mth frequency $\kappa_n^{(m)} = -i\omega^{(m)}/2a_i a_j$ is known (see [29]). It depends on two quantities: 1) the root-power wave a_i ($\text{W}^{1/2}$) exciting the ith port when the ith antenna operates in a transmitting mode and 2) the root-power wave a_j ($\text{W}^{1/2}$) exciting the jth port that feeds the Tx antenna. The physical meaning of the root-power waves is explained in [30]. As an example, if the field phasors in (1) are root-mean-square phasors, then a_i is the square root of the power injected into port i. Note that an S-parameter is associated with a particular mode of the ith port and a_i relates to the power of that mode only. Further, $\Delta\varepsilon_{\text{OBJ}}(\mathbf{r}')$ is the *relative* permittivity contrast

$$\Delta\varepsilon_{\text{OBJ}}(\mathbf{r}') = \varepsilon_{\text{OBJ}}(\mathbf{r}') - \varepsilon_{\text{RO}}(\mathbf{r}'). \quad (2)$$

In (1) and (2), OBJ (object) stands for CO (calibration object) or OUT (object under test). The scatterer-free measurement setup is referred to as the reference object (RO). Here, the permittivity contrast is assumed frequency-independent. However, if the dispersion relation is known and separable from the spatial dependence, it can be easily incorporated in the resolvent kernel [28].

There are two important advantages of the data equation (1) in comparison with the commonly used data equation where the data are the **E**-field values. First, it eliminates the need to approximate Green's dyadic. Green's dyadic is now reduced to Green's vector function [29], here $\mathbf{E}_{\text{RO},i}^{(m)}(\mathbf{r}'; \mathbf{r})$. In this

form, Green's function can be accurately obtained via simulations or measurements [29]. Second, it states the scattering model in terms of the measured S-parameters directly. Thus, there is no need to approximate the relationship between the field in the antenna vicinity and the S-parameter at its terminals.

The kernel in (1) consists of two field distributions. The first, $\mathbf{E}_{\text{RO},i}^{(m)}$, represents the incident field that would be generated by the ith Rx antenna in the nth experiment if this antenna operated in a Tx mode. On the other hand, $\mathbf{E}_{\text{OBJ},j}^{(m)}$ is the total internal field produced by the jth Tx antenna in the nth experiment.

By definition, the CO consists of a single voxel-size scatterer (the scattering probe) of known relative permittivity contrast $\delta\varepsilon_{\text{CO}}$ embedded in the RO. Let V' be uniformly discretized into N_v voxels of volume Ω_v and let the scattering probe reside at the pth voxel ($p = 1, \ldots, N_v$), the position of which is given by $\mathbf{r}'_p \in V'$. Assuming constant field inside the probe, its nth scattered response

$$\Delta S_{\text{CO},n,\mathbf{r}'_p}^{(m)}(\mathbf{r}) = S_{\text{CO},n,\mathbf{r}'_p}^{(m)}(\mathbf{r}) - S_{\text{RO},n}^{(m)}(\mathbf{r}) \quad (3)$$

is obtained from (1) as

$$\Delta S_{\text{CO},n,\mathbf{r}'_p}^{(m)}(\mathbf{r}) \approx \kappa_n^{(m)} \delta\varepsilon_{\text{CO}} \Omega_v \left[\mathbf{E}_{\text{RO},i}^{(m)}(\mathbf{r}'_p; \mathbf{r}) \cdot \mathbf{E}_{\text{CO},j}^{(m)}(\mathbf{r}'_p; \mathbf{r}) \right]. \quad (4)$$

The expression in (4) represents the point-spread function (PSF) of the nth response of the imaging system.

To express the total field $\mathbf{E}_{\text{CO}}$ in the scattering probe in terms of the incident field $\mathbf{E}_{\text{RO}}$, we utilize the localized quasi-linear (LQL) approximation, which assumes that the total field within an electrically small scatterer is proportional to the incident field via a reflectivity tensor $\bar{\bar{\lambda}}$ [31], [32]

$$\mathbf{E}_{\text{CO},j}^{(m)}(\mathbf{r}'_p; \mathbf{r}) \approx \bar{\bar{\lambda}}_{\text{CO}}^{(m)}(\mathbf{r}'_p) \cdot \mathbf{E}_{\text{RO},j}^{(m)}(\mathbf{r}'_p; \mathbf{r}). \quad (5)$$

Note that (5) is similar to the localized nonlinear approximation, which employs the depolarization tensor $\bar{\bar{\Gamma}}$ instead of $\bar{\bar{\lambda}}$ [33], [34]. These two quantities are formally related by a linear relationship [31]. What is important here is that the localized nonlinear approximation is most suitable for the scenarios when the internal field is a smoothly varying function of position, which is not the case with near-field imaging.

We assume that the total field $\mathbf{E}_{\text{CO}}$ inside the scattering probe is collinear with the incident field $\mathbf{E}_{\text{RO}}$. In this case, $\bar{\bar{\lambda}}_{\text{CO}}$ is expressed through a coefficient λ_{CO} as

$$\bar{\bar{\lambda}}_{\text{CO}} = \lambda_{\text{CO}} \bar{\bar{\mathbf{I}}}. \quad (6)$$

Substituting (6) into (4) leads to

$$\left[\mathbf{E}_{\text{RO},i}^{(m)}(\mathbf{r}'_p; \mathbf{r}) \cdot \mathbf{E}_{\text{RO},j}^{(m)}(\mathbf{r}'_p; \mathbf{r}) \right]_{\text{LQL}} \approx \frac{\Delta S_{\text{CO},n,\mathbf{r}'_p}^{(m)}(\mathbf{r})}{\kappa_n^{(m)} \delta\varepsilon_{\text{CO}} \Omega_v \lambda_{\text{CO}}^{(m)}}. \quad (7)$$

The above is the LQL resolvent kernel of the forward model specific to the nth response of the imaging system.

Next, the forward model (1) is applied to the OUT data

$$\Delta S_{\text{OUT},n}^{(m)}(\mathbf{r}) = \kappa_n^{(m)} \int_{V'} \Delta\varepsilon_{\text{OUT}}(\mathbf{r}')$$
$$\times \left[\mathbf{E}_{\text{RO},i}^{(m)}(\mathbf{r}'; \mathbf{r}) \cdot \mathbf{E}_{\text{OUT},j}^{(m)}(\mathbf{r}'; \mathbf{r}) \right] d\mathbf{r}'. \quad (8)$$

Neglecting the mutual coupling between the scattering voxels in the OUT, the LQL approximation is applied to (8) to obtain

$$\Delta S_{\text{OUT},n,\text{LQL}}^{(m)}(\mathbf{r}) \approx \kappa_n^{(m)} \int_{V'} \Delta \varepsilon_{\text{OUT}}(\mathbf{r}') \lambda_{\text{OUT}}^{(m)}(\mathbf{r}')$$
$$\times \left[\mathbf{E}_{\text{RO},i}^{(m)}(\mathbf{r}';\mathbf{r}) \cdot \mathbf{E}_{\text{RO},j}^{(m)}(\mathbf{r}';\mathbf{r}) \right]_{\text{LQL}} d\mathbf{r}'. \quad (9)$$

The substitution of (7) into (9) with $\mathbf{r}'_p \equiv \mathbf{r}'$ leads to

$$\Delta S_{\text{OUT},n,\text{LQL}}^{(m)}(\mathbf{r}) \approx \int_{V'} \Delta \varepsilon_{\text{OUT}}(\mathbf{r}') \lambda_{\text{OUT}}^{(m)}(\mathbf{r}') \left[\frac{\Delta S_{\text{CO},n,\mathbf{r}'}^{(m)}(\mathbf{r})}{\delta \varepsilon_{\text{CO}} \Omega_{\text{v}} \lambda_{\text{CO}}^{(m)}} \right] d\mathbf{r}'. \quad (10)$$

Note that all the quantities in the square brackets of (10) are known and they inherently incorporate the Green function of the specific imaging setup.

B. LQL *Rytov Approximation*

It is well known that the original Rytov approximation outperforms Born approximation when electrically large low-contrast objects are imaged since the accuracy of the Rytov approximation does not depend on the scatterer's size [33], [35]. Here, we derive the LQL Rytov (LQLR) approximation for the data equation using the LQL approximation of the CO internal field (5). In general, the LQLR approximation is expected to provide additional phase corrections to the simpler LQL approximation in the case of electrically large scatterers.

The LQLR approximation can be expressed in terms of the LQL approximation in the following way [36]:

$$S_{\text{OBJ},n,\text{LQLR}}^{(m)}(\mathbf{r}) \approx S_{\text{RO},n}^{(m)}(\mathbf{r}) \exp \left[\frac{\Delta S_{\text{OBJ},n,\text{LQL}}^{(m)}(\mathbf{r})}{S_{\text{RO},n}^{(m)}(\mathbf{r})} \right]. \quad (11)$$

In the case of $\text{OBJ} \equiv \text{CO}$, where the scattering probe is at $\mathbf{r}'$, we set $S_{\text{OBJ},n,\text{LQLR}}^{(m)}(\mathbf{r}) = S_{\text{CO},n,\mathbf{r}'}^{(m)}(\mathbf{r})$ and rearrange to obtain

$$\Delta S_{\text{CO},n,\text{LQL},\mathbf{r}'}^{(m)}(\mathbf{r}) \approx S_{\text{RO},n}^{(m)}(\mathbf{r}) \ln \left[\frac{S_{\text{CO},n,\mathbf{r}'}^{(m)}(\mathbf{r})}{S_{\text{RO},n}^{(m)}(\mathbf{r})} \right]. \quad (12)$$

Using (4)–(6), the nth CO scattered response for a scattering probe at $\mathbf{r}'$ at the mth frequency is obtained as

$$\Delta S_{\text{CO},n,\mathbf{r}',\text{LQL}}^{(m)}(\mathbf{r}) = \kappa_n^{(m)} \delta \varepsilon_{\text{CO}} \Omega_{\text{v}} \lambda_{\text{CO}}^{(m)}$$
$$\times \left[\mathbf{E}_{\text{RO},i}^{(m)}(\mathbf{r}';\mathbf{r}) \cdot \mathbf{E}_{\text{RO},j}^{(m)}(\mathbf{r}';\mathbf{r}) \right]. \quad (13)$$

It follows from (12) and (13) that the LQLR resolvent kernel can be expressed as

$$\left[\mathbf{E}_{\text{RO},i}^{(m)}(\mathbf{r}';\mathbf{r}) \cdot \mathbf{E}_{\text{RO},j}^{(m)}(\mathbf{r}';\mathbf{r}) \right]_{\text{LQLR}}$$
$$\approx \frac{S_{\text{RO},n}^{(m)}(\mathbf{r}) \cdot \ln \left[S_{\text{CO},n,\mathbf{r}'}^{(m)}(\mathbf{r})/S_{\text{RO},n}^{(m)}(\mathbf{r}) \right]}{\kappa_n^{(m)} \delta \varepsilon_{\text{CO}} \Omega_{\text{v}} \lambda_{\text{CO}}^{(m)}}. \quad (14)$$

Finally, to obtain the expression for the forward model of scattering under the LQLR approximation, we use the expression of the LQL forward model (9) and replace its resolvent kernel with that from (14) as

$$S_{\text{RO},n}^{(m)}(\mathbf{r}) \cdot \ln \left[\frac{S_{\text{OUT},n}^{(m)}(\mathbf{r})}{S_{\text{RO},n}^{(m)}(\mathbf{r})} \right]$$
$$\approx \int_{V'} \Delta \varepsilon_{\text{OUT}}(\mathbf{r}') \times \lambda_{\text{OUT}}^{(m)}(\mathbf{r}')$$
$$\times \left[\frac{S_{\text{RO},n}^{(m)}(\mathbf{r}) \cdot \ln \left(S_{\text{CO},n,\mathbf{r}'}^{(m)}(\mathbf{r})/S_{\text{RO},n}^{(m)}(\mathbf{r}) \right)}{\delta \varepsilon_{\text{CO}} \Omega_{\text{v}} \lambda_{\text{CO}}^{(m)}} \right] d\mathbf{r}'. \quad (15)$$

Note that we write the expression for $\Delta S_{\text{OUT},n,\text{LQL}}^{(m)}(\mathbf{r})$ on the left-hand side of (15) explicitly. For that, (11) is rearranged similar to (12), but with $\text{OBJ} \equiv \text{OUT}$ and $S_{\text{OBJ},n,\text{LQLR}}^{(m)}(\mathbf{r}) = S_{\text{OUT},n}^{(m)}(\mathbf{r})$. Also, note that the left-hand side as well as all the quantities in the square brackets on the right-hand side of (15) are known, which allows formulating a respective system of equations for the unknown distribution $\Delta \varepsilon_{\text{OUT}}(\mathbf{r}')$, $\mathbf{r}' \in V'$.

C. Power Maps

Henceforth, for the sake of brevity, all the theory is presented only for the case of the LQL approximation, thus the subscript LQL is omitted. The application of the LQLR approximation follows similar steps.

As shown in [24], the closer $\delta \varepsilon_{\text{CO}}$ is to $\Delta \varepsilon_{\text{OUT}}(\mathbf{r}')$, the closer the ratio $\lambda_{\text{OUT}}^{(m)}(\mathbf{r}')/\lambda_{\text{CO}}^{(m)}$ is to unity. Assuming that

$$\lambda_{\text{OUT}}^{(m)}(\mathbf{r}')/\lambda_{\text{CO}}^{(m)} \approx 1 \quad (16)$$

and discretizing the integral in the data equation (10) into a sum over all N_{v} voxels, (10) is written in the discrete form

$$\Delta S_{\text{OUT},n}^{(m)}(\mathbf{r}) \approx \sum_{q=1}^{N_{\text{v}}} \tau_q \Delta S_{\text{CO},n,\mathbf{r}'_q}^{(m)}(\mathbf{r}) \quad (17)$$

where

$$\tau_q = \Delta \varepsilon_{\text{OUT}}(\mathbf{r}'_q)/\delta \varepsilon_{\text{CO}}, \quad q = 1, \ldots, N_{\text{v}}. \quad (18)$$

As proposed in [24], the OUT power map is defined as a qualitative measure of the scattering occurring at each pth voxel $p = 1, \ldots, N_{\text{v}}$. Its value at $\mathbf{r}'_p \in V'$ for the mth frequency is determined via the CO responses with the scattering probe being at $\mathbf{r}'_p$, i.e., $S_{\text{CO},n,\mathbf{r}'_p}^{(m)}(\mathbf{r})$, $n = 1, \ldots, N_{\text{r}} \cdot N_{\text{t}}$. Let all responses (both CO and OUT) be measured on a discrete grid over the acquisition surface, where the observation location is indicated by the indices u and v, i.e., $\mathbf{r} \equiv \mathbf{r}_{uv}$. For example, in a rectangular planar scan of $N_x \cdot N_y$ grid points, $u = 1, \ldots, N_x$ and $v = 1, \ldots, N_y$. The value of the OUT power map $M_{\text{OUT}}^{(m)}$ at $\mathbf{r}'_p$ is defined as

$$M_{\text{OUT}}^{(m)}(\mathbf{r}'_p) = \sum_{n=1}^{N_{\text{t}} \cdot N_{\text{r}}} \sum_{u=1}^{N_x} \sum_{v=1}^{N_y} \Delta S_{\text{OUT},n}^{(m)}(\mathbf{r}_{uv})$$
$$\cdot \left[\Delta S_{\text{CO},n,\mathbf{r}'_p}^{(m)}(\mathbf{r}_{uv}) \right]^*, \quad p = 1, \ldots, N_{\text{v}}. \quad (19)$$

Note that (19) can produce a qualitative OUT image very fast without solving any systems of equations. However, the SPM method can be taken one step further to produce a quantitative image.

Substituting (17) into (19) leads to a linear system of equations in the unknown contrast distribution τ_q, $q = 1, \ldots, N_v$, which is explicitly written as

$$M_{\text{OUT}}^{(m)}(\mathbf{r}_p') = \sum_{n=1}^{N_t N_r} \sum_{q=1}^{N_v} \sum_{u=1}^{N_x} \sum_{v=1}^{N_y} \tau_q \Delta S_{\text{CO},n,\mathbf{r}_q'}^{(m)}(\mathbf{r}_{uv})$$
$$\cdot \left[\Delta S_{\text{CO},n,\mathbf{r}_p'}^{(m)}(\mathbf{r}_{uv})\right]^*, \quad p = 1, \ldots, N_v. \quad (20)$$

In matrix form

$$A^{(m)}\boldsymbol{\tau} = \boldsymbol{b}^{(m)} \quad (21)$$

where

$$A^{(m)} = \begin{bmatrix} M_{\text{CO},1}^{(m)}(\mathbf{r}_1') & \cdots & M_{\text{CO},N_v}^{(m)}(\mathbf{r}_1') \\ \vdots & & \vdots \\ M_{\text{CO},1}^{(m)}(\mathbf{r}_{N_v}') & \cdots & M_{\text{CO},N_v}^{(m)}(\mathbf{r}_{N_v}') \end{bmatrix} \quad (22)$$

$$\boldsymbol{\tau} = [\, \tau_1 \quad \cdots \quad \tau_{N_v} \,]^T \quad (23)$$

$$\boldsymbol{b}^{(m)} = [\, M_{\text{OUT}}^{(m)}(\mathbf{r}_1') \quad \cdots \quad M_{\text{OUT}}^{(m)}(\mathbf{r}_{N_v}') \,]^T. \quad (24)$$

Here, $M_{\text{CO},q}^{(m)}(\mathbf{r}_p')$, $q = 1, \ldots, N_v$, $p = 1, \ldots, N_v$, are CO power maps defined as

$$M_{\text{CO},q}^{(m)}(\mathbf{r}_p') = \sum_{n=1}^{N_t \cdot N_r} \sum_{u=1}^{N_x} \sum_{v=1}^{N_y} \Delta S_{\text{CO},n,\mathbf{r}_q'}^{(m)}(\mathbf{r}_{uv})$$
$$\cdot \left[\Delta S_{\text{CO},n,\mathbf{r}_p'}^{(m)}(\mathbf{r}_{uv})\right]^* \quad (25)$$

which is analogous to the OUT power map defined in (19). Note that when $p = q$, (25) becomes

$$M_{\text{CO},p}^{(m)}(\mathbf{r}_p') = \sum_{n=1}^{N_t \cdot N_r} \sum_{u=1}^{N_x} \sum_{v=1}^{N_y} \left|\Delta S_{\text{CO},n,\mathbf{r}_p'}^{(m)}(\mathbf{r}_{uv})\right|^2. \quad (26)$$

The power maps are pivotal in the SPM method, hence its name. The value of a power map at $\mathbf{r}_p'$ [see (19) or (25)] provides a measure of the similarity between the OUT responses and those of the CO obtained with the scattering probe at $\mathbf{r}_p'$. This measure corresponds to a cross-correlation in the time domain. On the other hand, the CO power map value at $\mathbf{r}_p'$, when the scattering probe is at $\mathbf{r}_p'$, represents the maximum attainable scattered power among all voxels [see (26)], which is expressed as the sum of the autocorrelations of all responses. More insights into the power-map concept can be found in [24].

The $N_v \times N_v$ matrix $A^{(m)}$ in (21) consists of the CO power maps formed using (25). The $N_v \times 1$ vector $\boldsymbol{b}^{(m)}$ contains the OUT power map formed using (19). Solving (21) for $\boldsymbol{\tau}$ allows to estimate a relative permittivity contrast $\Delta \varepsilon_{\text{OUT}}(\mathbf{r}_p')$ from (18). Finally, an actual relative permittivity distribution of the OUT is obtained from (2).

D. Application to Frequency-Swept Data

Often, microwave imaging employs multifrequency data. In this case, the multifrequency power maps are added after the following normalization procedure [24], [37]:

$$M_{\text{OBJ}}(\mathbf{r}_p') = \frac{1}{N_f} \sum_{m=1}^{N_f} \frac{|M_{\text{OBJ}}^{(m)}(\mathbf{r}_p')|}{\eta^{(m)}} \cdot e^{i \angle M_{\text{OBJ}}^{(m)}(\mathbf{r}_p')} \quad (27)$$

where $\eta^{(m)}$ is the maximum magnitude value of the CO power map at the mth frequency

$$\eta^{(m)} = \max \left(|M_{\text{CO},q}^{(m)}(\mathbf{r}_p')|\right). \quad (28)$$

Note that the normalization strategy in (27) preserves the phase of each single-frequency power map. The normalization factor $\eta^{(m)}$ in (27) can be calculated using strategies alternative to (28), e.g., using the energy normalization [15]. However, (28) offers simpler implementation and faster computation [37].

The CO power maps across all frequencies are also combined using (27) to form the multifrequency matrix A. Similarly, the vector $\boldsymbol{b}$ is formed using the frequency-combined OUT power map. The size of the so-obtained linear system of equations $A\boldsymbol{\tau} = \boldsymbol{b}$ is independent of the number of frequency points.

E. Planar Coordinate Translation

If the imaging system is invariant to lateral translations, the experimentally obtained PSF in (4) with a scattering probe at the center of the imaged volume can be used to obtain the PSFs at all other lateral positions $\mathbf{r}_p' \in V'$. This can be realized by coordinate translation.

In [24] and [25], it was suggested to perform the CO scan over an area A_{CO}, which is four times larger than the area A' used to acquire the data for an OUT. This concept is illustrated in Fig. 1 with two examples of voxels to be imaged. Each element of the square grid indicates a sampling position, which is also an imaged voxel. Fig. 1(a) and (c) shows the cross-sectional area of the OUT. In Fig. 1(a), the central voxel P_{center} is highlighted, whereas in Fig. 1(c), the corner voxel P_{corner} is indicated by a thick line. Fig. 1(b) and (d) shows the entire area A_{CO} scanned in the calibration CO measurement. In this measurement, the scattering probe is fixed at the origin O while the antennas sample the response over A_{CO}. The CO response subset acquired in the area $A'_{P_{\text{center}}}$ [outlined with a solid line in Fig. 1(b)] is $\Delta S_{\text{CO},n,P_{\text{center}}}^{(m)}(\mathbf{r})$, $\mathbf{r} \in A'_{P_{\text{center}}}$. This is the PSF used to compute the value of the OUT power map at P_{center} with (19), wherein $\mathbf{r}_p' \equiv P_{\text{center}}$ [see Fig. 1(a)]. On the other hand, the CO response subset $\Delta S_{\text{CO},n,P_{\text{corner}}}^{(m)}(\mathbf{r})$, $\mathbf{r} \in A'_{P_{\text{corner}}}$, acquired in the area $A'_{P_{\text{corner}}}$ [outlined with a solid line in Fig. 1(d)] is the PSF used to compute the value of the OUT power map at $\mathbf{r}_p' \equiv P_{\text{corner}}$.

Here, we propose to eliminate the need for four times larger CO scan by exploiting the shift property of the Fourier transform. Let $\mathbf{r}_0'(\bar{z}') \equiv P_{\text{center}}$ denote the center of the fixed range plane $\bar{z}'$ in which the scattering probe resides. Let the PSF shift along x and y with respect to $\mathbf{r}_0'(\bar{z}')$ be expressed with multiples of the respective sampling steps Δx and Δy as

$$\Delta \mathbf{r}_{uv}(\bar{z}') = (u\Delta x, v\Delta y), \quad u = 1, \ldots, N_x; \; v = 1, \ldots, N_y. \quad (29)$$

Then, the values of the shifted PSFs

$$\Delta S_{\text{CO},n,\mathbf{r}_0'(\bar{z}') - \Delta \mathbf{r}_{uv}'(\bar{z}')}^{(m)}(x, y), \quad u = 1, \ldots, N_x; \; v = 1, \ldots, N_y \quad (30)$$
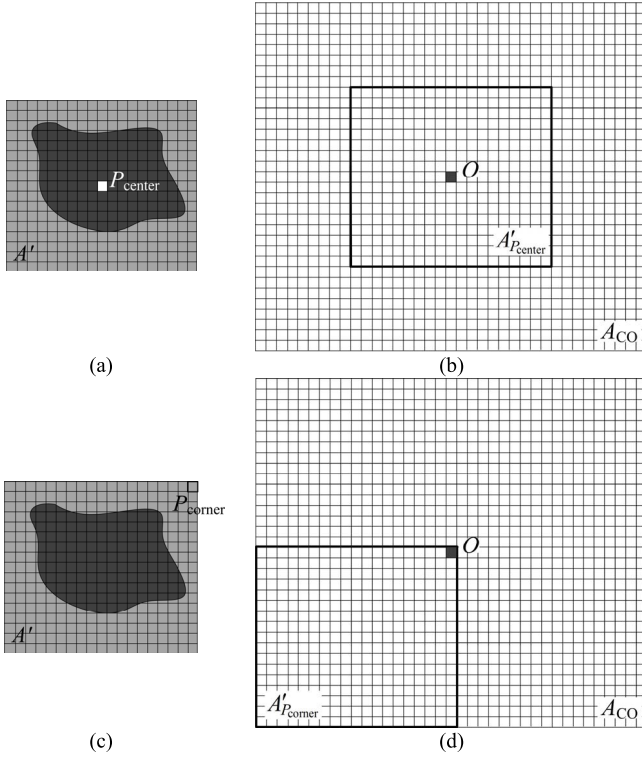
Fig. 1. Illustration of the measured S-parameter data on a square sampling grid. (a) OUT area A' with an imaged voxel P_{center} at the center. (b) CO area A_{CO} and its portion $A'_{P_{center}}$ used to image the voxel P_{center}. (c) OUT area A' with an imaged voxel P_{corner} at the corner. (d) CO area A_{CO} and its portion $A'_{P_{corner}}$ used to image the voxel P_{corner}. The origin of CO area, which is also the position of the scattering probe, is denoted as O.

can be obtained from that of $\Delta S_{CO,n,\mathbf{r}'_0(\bar{z}')}^{(m)}(x, y)$ using

$$\Delta S_{CO,n,\mathbf{r}'_0(\bar{z}')-\Delta\mathbf{r}'_{uv}(\bar{z}')}^{(m)}(x, y)$$
$$= \mathcal{F}_{2\text{-}D}^{-1}\{\mathcal{F}_{2\text{-}D}\{\Delta S_{CO,n,\mathbf{r}'_0(\bar{z}')}^{(m)}(x, y)\}e^{-\mathbf{i}k_x u\Delta x}e^{-\mathbf{i}k_y v\Delta y}\}. \quad (31)$$

Here, k_x and k_y are the Fourier variables corresponding to x and y, respectively. With this approach, the CO scan area matches that of the OUT.

F. BCCB Solver

Utilizing the k-space coordinate translation has yet another advantage—the SPM system matrix $A \in \mathbb{C}^{N_v \times N_v}$, $N_v = N_x N_y$ becomes block circulant with circulant blocks, or BCCB. When the number of range samples N_z is larger than one (3-D imaging), we have $N_v = N_x N_y N_z$ and the matrix A becomes block circulant with BCCB blocks. We emphasize that the CO in either case does not have to be symmetrical ($N_x \neq N_y$). If A is block circulant with BCCB blocks (which is the most general case), the following holds [26], [27]:

$$A = F^{-1}\text{diag}(\text{vec}(\hat{a}))F \quad (32)$$

where the Fourier matrix $F \in \mathbb{C}^{N_v \times N_v}$ is found from the Kronecker tensor product $F = F_z \otimes F_y \otimes F_x$ ("outside" to "inside" order) with F_z, F_y, and F_x being Fourier matrices of size $N_z \times N_z$, $N_y \times N_y$ and $N_x \times N_x$, respectively. The

linear operator $\text{vec} : \mathbb{C}^{N_x \times N_y \times N_z} \rightarrow \mathbb{C}^{N_v}$ produces a vector by stacking the columns of $\hat{a}$, where the components of $\hat{a}$ are the eigenvalues of A found from

$$\hat{a} = \sqrt{N_v}\mathcal{F}_{2\text{-}D(3\text{-}D)}\{\text{array}(a)\}. \quad (33)$$

Here, the symbol $\text{array} : \mathbb{C}^{N_v} \rightarrow \mathbb{C}^{N_x \times N_y \times N_z}$ denotes the inverse of the vec operator, whereas a is the first column of A. Also, since the Fourier matrix F is unitary, its inverse in (32) is readily calculated as

$$F^{-1} = (N_v)^{-1}F^{\dagger}. \quad (34)$$

From (32) it follows that there is no need to construct the whole matrix of CO power maps as per (22). Furthermore, nonsingular BCCB systems can be solved using the following recipe [27]:

$$\tau = \text{vec}(\mathcal{F}_{2\text{-}D(3\text{-}D)}^{-1}\{\mathcal{F}_{2\text{-}D(3\text{-}D)}\{\text{array}(b)\}./\hat{a}\}) \quad (35)$$

where "./" means componentwise division of the 2-D (or 3-D) arrays.

Note that the solution τ in (35) is obtained only from the first column of A. Utilizing 2-D (or 3-D) FFT in (35) allows to solve the system of equations (21) at a $O(N_v \log(N_v))$ cost. Thus, there is no need to invert a matrix at the typical cost of $O(N_v^3)$. There is no need to perform a matrix-vector multiplication either at a $O(2N_v)$ cost. Moreover, due to the ill-posed nature of an inverse problem, the CO power maps matrix A is usually ill-conditioned. Convergence rates for the solution schemes based on the conjugate-gradient method depend on the singular values of A. On the other hand, the solution with (35) is performed in real time since it is expedited by the 2-D (or 3-D) FFT. This is possible due to the advantage of having the BCCB structure. Finally, we remark that Tikhonov regularization is applicable with the BCCB system. It results in a system that can be solved directly using 2-D (or 3-D) FFTs without computational overhead in a manner similar to (35) [27].

G. Limitations of the Method

The major limitation of the SPM, which is typical for all direct-inversion methods, is its inability to account for the mutual coupling and multiple scattering present in the OUT. For example, reconstruction of a complex object comprised of high-contrast layers with embedded scatterers of varying dielectric permittivity is likely to fail. That is why SPM can be used either in weak-scattering problems or as a module within nonlinear iterative methods such as the Born iterative method and the distorted Born iterative method.

In general, the accuracy of the LQL approximation and LQLR approximation used in SPM is a function of frequency and the size of the imaged target as discussed earlier in Section II-B. Also, in order for (16) to hold, the relative permittivity of the CO should be close to that of the OUT. This condition ensures the accurate quantitative reconstruction and serves as a guideline when choosing the properties of the CO. We remark that the fidelity of the qualitative reconstruction with (19) is not dependent on the relative permittivity of the CO.

We assume that the total field within a scattering probe has the same polarization as the incident field. Thus, the assumption in (6) is clearly not always valid either in the case of the CO, or in the case of the OUT. The more accurate approximation of the internal field can be achieved using more complex reflectivity tensors, such as the diagonal reflectivity tensor [32].

Finally, it should be emphasized that if the CO cannot be reconstructed, the OUT would not be imaged either since the CO response represents the PSF of each particular imaging setup. Therefore, the size of a scattering probe should be large enough for the imaging system to detect its response and small enough to ensure approximately uniform internal field distribution as dictated by (4). The lateral size of the scattering probe must be smaller than $\lambda/4$, where λ is the shortest wavelength inside the CO. As for the vertical dimension, it should be approximately the same as the thickness of the measured spatial step along the range.

III. SPM VALIDATION

A. Two Dielectric Cylinders Embedded in Absorbers

The first validation example is similar to that presented in [24] when two dielectric objects embedded in absorber sheets are imaged. We commence with such an example in order to demonstrate the capabilities of the proposed SPM compared to those of the prior method.

The specifics of the imaged setup are the same as in the experiment reported in [24]. The frequency sweep is from 3 to 9 GHz. The scanned area is 15 cm × 15 cm with a 5-mm spatial step. The RO consists of five absorber sheets being 20 cm × 20 cm by 1 cm in size, with relative permittivity of $\varepsilon_{RO} \approx 10 - i5$. The CO is identical to the RO except for a dielectric cylinder of $\varepsilon_{sc} \approx 15 - i0.003$ [38] embedded in the center of the middle layer. The cylinder is 1 cm in height and 1 cm in diameter. Finally, the OUT is identical to the RO except for two such dielectric cylinders separated by 1 cm, and embedded in the middle layer. Note that only transmission S-parameters are acquired because a power amplifier is connected directly to the transmitting antenna [24].

The reconstructed results of the OUT (middle layer) are shown in Fig. 2. Fig. 2(a) and (b) show the estimated permittivity distribution when the SPM forward model is linearized with the LQL approximation. Fig. 2(c) and (d) show the images obtained with the LQLR approximation. The BCCB solver with no regularization has been used in both cases. Since the experimental data contain considerable noise and positioning uncertainties, it is recommended to use a denoising algorithm [39].

We observe an improved fidelity of the reconstruction in Fig. 2 compared to the images shown in [24], at a much faster computational time of the order of seconds. The improvement comes from the BCCB structure of the system matrix. Also, we are now able to reconstruct the whole scanned area of 15 cm × 15 cm. This is compared to the imaged area of 5.5 cm × 5.5 cm in [24]. Note that utilizing the LQLR approximation is expected to produce similar images compared to those obtained with the LQL approximation, since
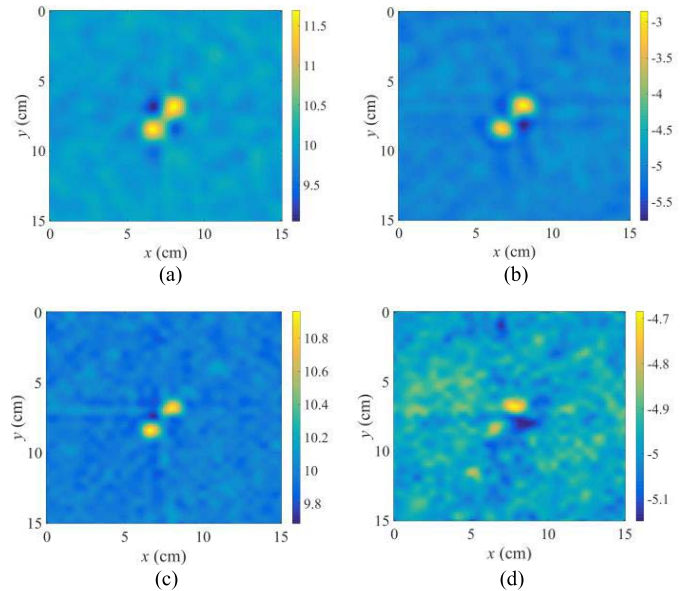

Fig. 2. Quantitative multifrequency images of two dielectric cylinders obtained with SPM showing the estimated relative permittivity. Results using the LQL approximation. (a) Real part. (b) Imaginary part. Results using the LQLR approximation. (c) Real part. (d) Imaginary part.

the size of the scatterers in the OUT is electrically small. On the other hand, the permittivity contrast is sufficiently large to violate the constraints of the Rytov approximation [40]. This explains the poorer reconstruction especially in the imaginary part of the relative permittivity [see Fig. 2(d)].

B. Synthetic Multilayered Object

As the next step, we perform the scan of a five-layer synthetic object with the setup shown in Fig. 3. The top and bottom OUT layers are made of a 3-mm dielectric sheet with $\varepsilon_r \approx 12$. The other three layers are $20 \times 20 \times 1$ cm^3 absorber sheets with a relative permittivity of $\varepsilon_r \approx 10 - i5$. The second layer from the bottom contains a dielectric cross of $\varepsilon_r \approx 18$, a dielectric cylinder of $\varepsilon_r \approx 12$ and four dielectric cylinders of $\varepsilon_r \approx 15 - i0.003$ [38]. All these objects are embedded in the absorbing material with $\varepsilon_r \approx 10 - i5$ [see Fig. 3(b)]. The third layer from the bottom does not contain inclusions. The fourth layer from the bottom contains dielectric cross of $\varepsilon_r \approx 12$ positioned at the center [see Fig. 3(c)]. All the cylinders used in this experiment are 1 cm in diameter and 1 cm in height.

Two TEM horn antennas [41] are aligned along each other's boresight and move in a planar raster fashion [see Fig. 3(a)]. The distance from the antennas' aperture to the OUT is 3 mm. The frequency sweep is from 3 GHz to 9 GHz with 61 frequency samples. The output power of the vector network analyzer (VNA) is 5 dBm. The imaged area is 13 cm × 13 cm with a 2-mm sampling step. Both reflection and transmission coefficients are acquired.

The RO is comprised of two dielectric sheets and three absorber sheets resembling the OUT's structure with no scattering objects. For the CO scan, we use a dielectric cylinder of 1-cm diameter and 1-cm height, with a relative permittivity of $\varepsilon_r \approx 15 - i0.003$. This cylinder is in succession embedded
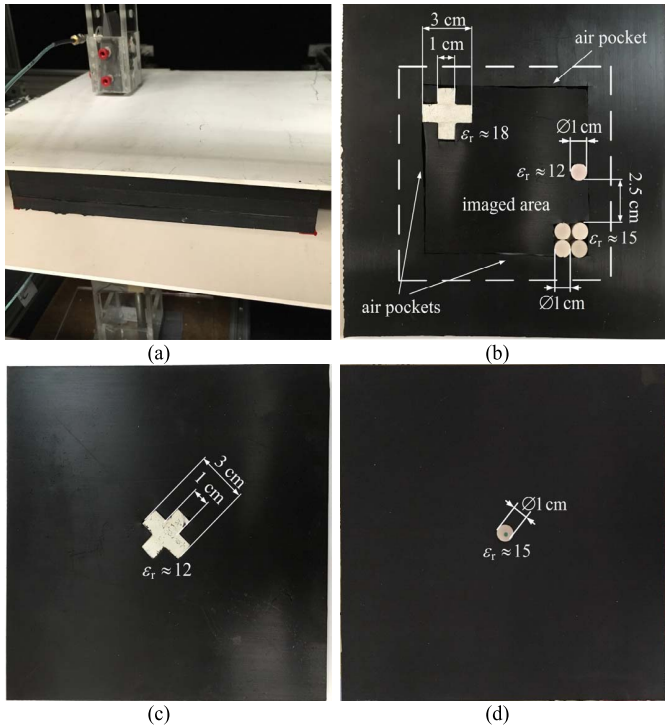
Fig. 3. Photographs of (a) imaging setup with five-layer OUT, (b) second (from the bottom) layer of OUT with 13 cm × 13 cm imaged area (dashed white line), (c) fourth (from the bottom) layer of OUT with a dielectric cross, and (d) CO layer with a dielectric cylinder serving as a scattering probe.

at the center of each of the three absorber sheets comprising the RO. These are the three CO measurements, which provide the PSFs needed to generate the images at the corresponding range locations $z = 0.8$, 1.8, and 2.8 cm, with the origin being at the bottom of the OUT.

The reconstruction results obtained with the SPM employing the LQL approximation are shown in Fig. 4, whereas the LQLR results are shown in Fig. 5. We observe superior quality of the reconstruction in the case of the LQLR approximation, especially in the imaginary part of the OUT permittivity [see Figs. 4(b) and 5(b)]. Also, we are able to see the air pockets contained in the layer at $z = 0.8$ cm [see Fig. 5(a) and (b)].

This experiment also exemplifies the limitations of the proposed linear reconstruction methodology. The reconstructed real part of the OUT permittivity with both the LQL and LQLR approximations is not satisfactory [Figs. 4(a) and 5(a)]. This is due to two main factors. First, the scattering objects have much less contrast with the background (the RO) in the real part of the permittivity compared to the imaginary part. Second, the RO is layered, where the top and bottom low-loss slabs differ in their permittivity from the middle three layers, which have significant loss and lower permittivity. At the same time, the top and bottom slabs are right next to the inclusions, which lead to strong coupling with them. This effect cannot be captured by the measured PSFs (the CO measurements), neither can it be accounted for by the linearized inversions based on the LQL and the LQLR approximations.

C. Reconstruction of Living Tissue Samples

In the next example, we attempt the imaging of living tissue. The reconstruction of such a complex OUT is expected to
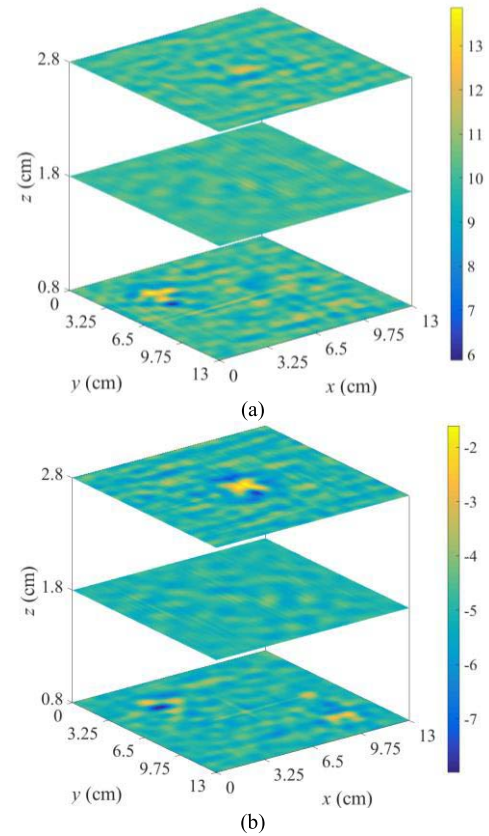

Fig. 4. Quantitative multifrequency images of five-layer OUT obtained with SPM. (a) Real and (b) imaginary parts of relative permittivity. LQL approximation is used.

test the limits of the SPM since they are violated by both the contrast and the size of the scattering object. The planar raster-scanning imaging setup used to acquire the S-parameter measurements is shown in Fig. 6. It consists of two TEM horn antennas [41] aligned along each other's boresight and moving together in a planar raster fashion. The frequency range is from 3 to 9 GHz with 61 frequency samples. The imaged area is 13 cm × 13 cm with 2-mm spatial sampling step. The VNA output power is 0 dBm.

The distance from the antennas' aperture to the inspected object on the platform is 3 mm. The OUT consists of pure lard together with a chicken wing embedded in an absorber sheet of size 20 cm × 20 cm × 1 cm [see Figs. 6 and 7(a)]. It is set on the 5-mm thick dielectric platform [42]. The RO is chosen to be an absorber sheet, whereas the CO contains a dielectric scatterer in the center of the RO [Fig. 7(b)]. The scatterer is a cylinder 5 mm in diameter and 10 mm high. The averaged relative permittivities of the objects used in the experiment are given in Table I.

Reconstruction results obtained with the SPM utilizing the LQL approximation and the BCCB solver are shown in Fig. 8. Although the OUT contours are somewhat visible [Fig. 8(a)], it is seen that the LQL model does not yield meaningful quantitative results. Moreover, employing (32) to solve the system $A\tau = b$ with another solver, the conjugate-gradient with circulant preconditioner (pcg function in MATLAB [43]
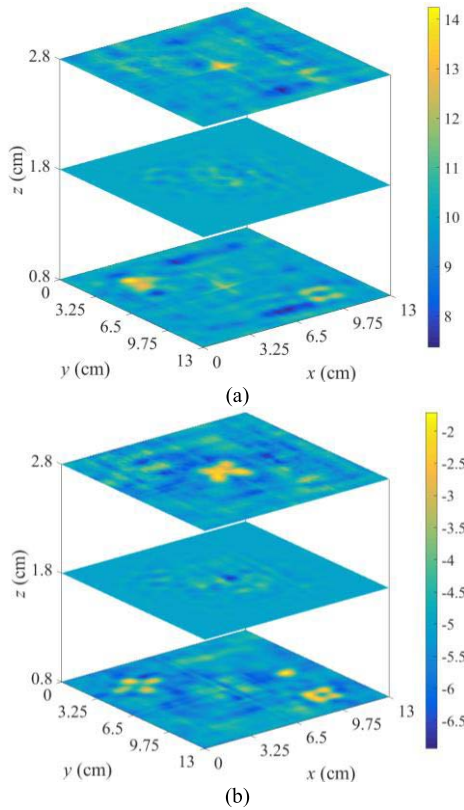
Fig. 5.   Quantitative multifrequency images of five-layer OUT obtained with SPM. (a) Real and (b) imaginary parts of relative permittivity. LQLR approximation is used.
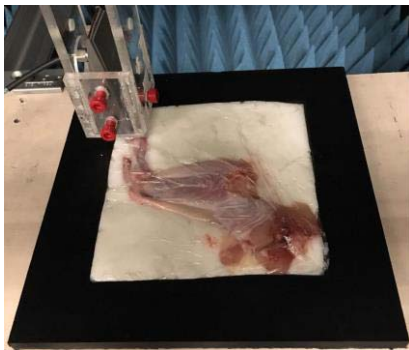

Fig. 6.   Photograph of the setup for the living tissue experiment.

and MATLAB Structured Matrices Toolbox [44]), produces similar images to those obtained with the BCCB solver.

On the other hand, LQLR approximation is observed to offer better fidelity of the reconstruction: the contours of the chicken wing are distinguishable and the quantitative values are correct (see Fig. 9). Better performance of the LQLR approximation is expected: the chicken wing is an electrically large object at the given frequencies. However, we notice some nonphysical values in the reconstructed images: it is especially noticeable in the imaginary part of the relative permittivity [Fig. 9(b)]. Note that these nonphysical values in the relative complex permittivity distributions for the LQL (Fig. 8) and LQLR (Fig. 9) approximations are close to each
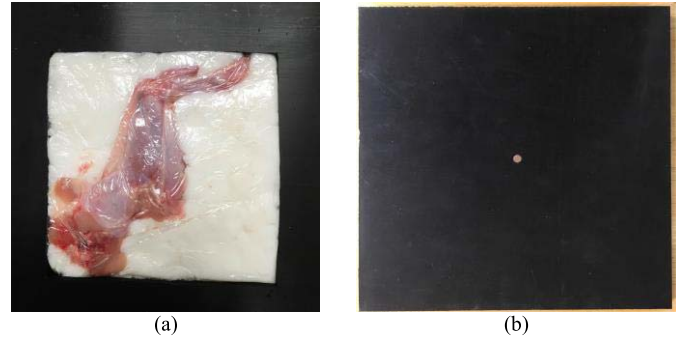

Fig. 7.   Photographs of (a) OUT and (b) CO used in the experiment.

TABLE I
AVERAGED RELATIVE PERMITTIVITIES IN TISSUE EXPERIMENT

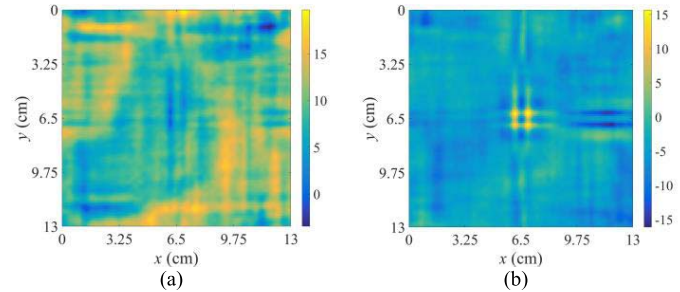| Object	Relative permittivity value, ε_r, averaged from 3 GHz to 9 GHz
Absorber sheet (RO)	$10-i5$
Lard	$3.1-i0.4$
Chicken skin	$14.4-i6.2$
Chicken bone	$21.5-i10.7$
Chicken muscle	$47.6-i25.9$
Scatterer in the CO	43.7
Dielectric platform	$10-i0.035$

Fig. 8.   Quantitative multifrequency images obtained with SPM using LQL approximation. (a) Real and (b) imaginary parts of relative permittivity. BCCB solver has been used. Only transmission data are processed.
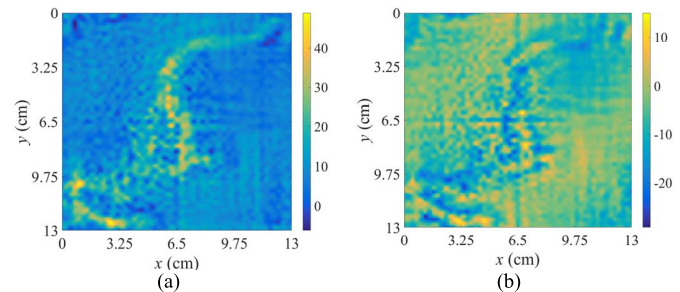

Fig. 9.   Quantitative multifrequency images obtained with SPM using LQLR approximation. (a) Real and (b) imaginary parts of relative permittivity. BCCB solver has been used. Only transmission data are processed.

other. There are a few possible causes of this problem: 1) the ill-posed nature of the inversion problem; 2) stochastic noise and measurement uncertainties present in the raw data; and 3) violation of the limitations of the forward model. The denois-
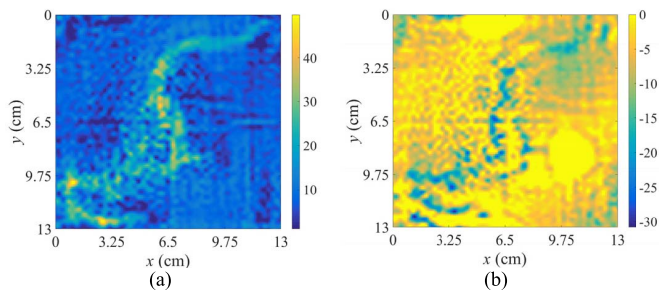
Fig. 10. Quantitative multifrequency images obtained with SPM using LQLR approximation. (a) Real and (b) imaginary parts of relative permittivity. Constrained linear least-squares solver has been used. Only transmission data are processed.
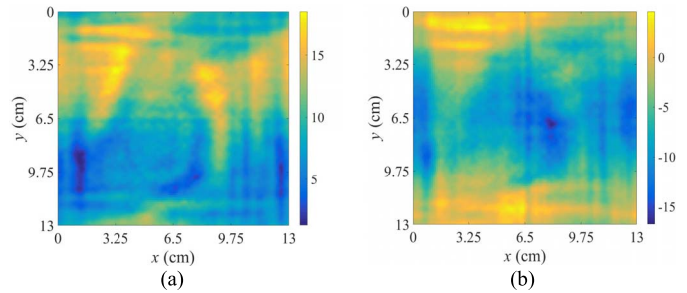

Fig. 11. Quantitative multifrequency images obtained with SPM using LQL approximation. (a) Real and (b) imaginary parts of relative permittivity. Denoising algorithm along with Gaussian apodization function has been used.

ing algorithm proposed in [39] is instrumental in reducing the nonphysical values substantially, but it cannot remove them completely. Therefore, the stochastic noise and measurement uncertainties alone are not responsible for this problem; it is rather a combination of different factors. Nonetheless, the most straightforward way to solve nonphysicality problem can be to impose the following constraints:

$$\begin{cases} \mathrm{Re}\big(\varepsilon_{\mathrm{OUT}}\big(\mathbf{r}'_p\big)\big) \geq 1 \\ \mathrm{Im}\big(\varepsilon_{\mathrm{OUT}}\big(\mathbf{r}'_p\big)\big) \leq 0 \end{cases}, \quad \mathbf{r}' \in V'. \tag{36}$$

However, this requires the use of another solver (e.g., constrained linear least-squares or semidefinite programming), which might significantly slow down the solution. Reconstruction example utilizing constrained linear least-squares solver (*lsqlin* function in Matlab) is shown in Fig. 10. The running time in this case is of the order of hours. We observe better image fidelity in case of the real part of the relative permittivity compared to that in Fig. 9(a). The imaginary part does not improve significantly [see Fig. 10(b)].

D. Signal-to-Noise Ratio of Measured Data

The signal-to-noise ratio (SNR) of the measured data has a significant impact on the reconstruction fidelity. For the experiment with two dielectric cylinders embedded in absorber sheets, the SNR ranges from about 10 dB at 3 GHz to 2 dB at 9 GHz as reported in [24]. An alternative way of calculating the data SNR is presented in [39], which effectively separates the data at each frequency into two additive components: signal and noise. The ratio of these components yields the data SNR. For the two-cylinder example, this method yields similar data SNR values as those reported in [24]. In the second experiment, the data SNR changes from about 14 dB at 3 GHz to 10.5 dB at 9 GHz. Finally, in the tissue experiment, the data SNR varies from 11 dB at 3 GHz to 7 dB at 9 GHz.

Increasing the number of the independent responses improves the SPM robustness to noise, i.e., imaging is successful with lower data SNR. This is achieved by increasing the number of the transmitters, the receivers, and the frequency samples [15], [16], [24]. The improved robustness to noise is due to the fact that the SPM qualitative maps (matrix $\mathbf{b}$) are, in essence, plots of the cross correlation of the OUT data with the system PSF. The cross-correlation peaks at voxels where scattering occurs. Moreover, with multiple data sets,

these peaks add coherently. In contrast, at voxels void of scatterers, the cross-correlation values across the data sets add incoherently thus enhancing the image SNR.

The denoising algorithm presented in [39] can substantially mitigate the detrimental effects of stochastic noise. Notably, the condition number of a system matrix $\mathbf{A}$ improves by a few orders of magnitude. For example, the condition number of the matrix $\mathbf{A}$ under the LQL approximation in the living tissue example drops from $6 \cdot 10^8$ to $8 \cdot 10^4$.

E. Central-Line Artifact

It is observed that the reconstructed images contain an artifact in the form of horizontal and vertical lines intersecting at the center of the image. This artifact occurs when a sampled signal does not smoothly go down to zero at the edges of the acquisition aperture. As a result, leakage sidelobes are produced upon performing a discrete Fourier transform, an effect known as apodization [45]. Such sidelobes can create ringing artifacts, which in our case appear as spurious lines at the center of the reconstructed images. These artifacts are usually mitigated by multiplying a signal in the spatial domain by a proper apodization function [46]. In order to demonstrate this effect, we employ the commonly used Gaussian apodization function to the reconstruction example affected strongly by the central-line artifact (see Fig. 8). The resultant images are presented in Fig. 11. Although the real part of the relative permittivity in Fig. 11(a) appears worse than that in Fig. 8(a), it does not contain central-line artifact nor nonphysical values. Moreover, the imaginary part in Fig. 11(b) is significantly improved: the OUT contours become visible and the nonphysical values are suppressed. Nevertheless, the LQL model does not yield satisfactory quantitative images in the tissue example, which illustrates its limitations.

IV. CONCLUSION

SPM is proposed as a direct-inversion method for fast quantitative imaging. It accommodates a forward model of scattering cast either as a linearized Born model or as a Rytov model. Two key advantages of the SPM compared to the work reported in [24] are the computational speed and the reduced area of the calibration scan. These advantages stem from the PSF coordinate translation implemented in the Fourier domain, which leads to the system matrix being of particular mathematical structure, namely, block circulant with

circulant blocks. This mathematical structure is exploited to reduce drastically the computational cost.

The calibration strategy currently used by the SPM imposes limitations. For accurate quantitative results, the permittivity of a voxel in the OUT must be close to that of the scattering probe in the CO. Since the permittivity of the scattering probe is fixed, the quantitative reconstruction of objects with widely varying permittivity distribution is not likely to be accurate. Note that the requirement for the OUT permittivity to be close to that of the scattering probe in the CO measurement is important for the quantitative accuracy of the imaging method; it does not affect the accuracy of the target localization and shape recovery. In order to achieve target-independent quantitative accuracy, we are currently developing a new calibration strategy employing a metallic scattering probe. It uses a theoretical model of scattering proposed in [29].

The Born or the Rytov approximations, which linearize the forward model, also impose limitations. The LQL (Born) or LQLR (Rytov) forward models are applicable to weakly scattering object with their respective constraints (see [13], [19]). They cannot account for multiple scattering or mutual coupling, which compromises the reconstruction in the case of strong scattering. However, due to its ability to produce quantitative images, the SPM can be used as a direct-inversion tool within a nonlinear iterative procedure, e.g., the Born iterative method [19].

The challenging example of living-tissue imaging clearly demonstrates the limitations of the SPM, although reconstruction of satisfactory fidelity is achievable due to the fact that SPM can accommodate the Rytov forward model. The Rytov model is not limited by the target's size; therefore, the LQLR-based SPM is more likely to succeed in the near-field imaging of large tissue samples.

REFERENCES

[1] R. Zoughi, Microwave Non-Destructive Testing and Evaluation. Dordrecht, The Netherlands: Kluwer, 2000.

[2] M. Pastorino, Microwave Imaging. Hoboken, NJ, USA: Wiley, 2010.

[3] M. G. Amin, Through-the-Wall Radar Imaging. Boca Raton, FL, USA: CRC Press, 2011.

[4] D. J. Daniels, EM Detection of Concealed Targets. Hoboken, NJ, USA: Wiley, 2009.

[5] L. E. Larsen and J. H. Jacobi, "Microwave interrogation of dielectric targets. Part I: By scattering parameters," Med. Phys., vol. 5, no. 6, pp. 500–508, 1978.

[6] L. E. Larsen and J. H. Jacobi, Medical Applications of Microwave Imaging. New York, NY, USA: IEEE Press, 1986.

[7] A. Rosen, M. A. Stuchly, and A. V. Vorst, "Applications of RF/microwaves in medicine," IEEE Trans. Microw. Theory Techn., vol. 50, no. 3, pp. 963–974, Mar. 2002.

[8] R. E. Sepponen, "Medical diagnostic microwave scanning apparatus," U.S. Patent 4641659, Feb. 10, 1987. [Online]. Available: http://www.google.com/patents/US4641659

[9] K. D. Paulsen, P. M. Meaney, and L. C. Gilman, Alternative Breast Imaging: Four Model-Based Approaches. Berlin, Germany: Springer, 2005.

[10] M. Elsdon, D. Smith, M. Leach, and S. J. Foti, "Experimental investigation of breast tumor imaging using indirect microwave holography," Microw. Opt. Technol. Lett., vol. 48, no. 3, pp. 480–482, Mar. 2006.

[11] D. M. Sheen, D. L. McMakin, and T. E. Hall, "Three-dimensional millimeter-wave imaging for concealed weapon detection," IEEE Trans. Microw. Theory Techn., vol. 49, no. 9, pp. 1581–1592, Sep. 2001.

[12] R. K. Amineh, M. Ravan, A. Khalatpour, and N. K. Nikolova, "Three-dimensional near-field microwave holography using reflected and transmitted signals," IEEE Trans. Antennas Propag., vol. 59, no. 12, pp. 4777–4789, Dec. 2011.

[13] A. J. Devaney, Mathematical Foundations of Imaging, Tomography and Wavefield Inversion. Cambridge, U.K.: Cambridge Univ. Press, 2012.

[14] P. Kosmas and C. M. Rappaport, "FDTD-based time reversal for microwave breast cancer detection-localization in three dimensions," IEEE Trans. Microw. Theory Techn., vol. 54, no. 4, pp. 1921–1927, Jun. 2006.

[15] L. Liu, A. Trehan, and N. K. Nikolova, "Near-field detection at microwave frequencies based on self-adjoint response sensitivity analysis," Inverse Prob., vol. 26, no. 10, pp. 1–28, Aug. 2010.

[16] Y. Zhang, S. Tu, R. K. Amineh, and N. K. Nikolova, "Resolution and robustness to noise of the sensitivity-based method for microwave imaging with data acquired on cylindrical surfaces," Inverse Prob., vol. 28, no. 11, pp. 1–15, Oct. 2012.

[17] E. C. Fear, X. Li, S. C. Hagness, and M. A. Stuchly, "Confocal microwave imaging for breast cancer detection: Localization of tumors in three dimensions," IEEE Trans. Biomed. Eng., vol. 49, no. 8, pp. 812–822, Aug. 2002.

[18] H. B. Lim, N. T. T. Nhung, E.-P. Li, and N. D. Thang, "Confocal microwave imaging for breast cancer detection: Delay-multiply-and-sum image reconstruction algorithm," IEEE Trans. Biomed. Eng., vol. 55, no. 6, pp. 1697–1704, Jun. 2008.

[19] W. C. Chew, Waves and Fields in Inhomogeneous Media. Piscataway, NJ, USA: IEEE Press, 1995.

[20] R. F. Remis and P. M. van den Berg, "On the equivalence of the Newton-Kantorovich and Distorted Born Methods," Inverse Prob., vol. 16, no. 1, pp. 1–4, Feb. 2000.

[21] Y. M. Wang and W. C. Chew, "An iterative solution of the two-dimensional electromagnetic inverse scattering problem," Int. J. Imag. Syst. Technol., vol. 1, no. 1, pp. 100–108, Jun. 1989.

[22] G. Bozza and M. Pastorino, "An inexact newton-based approach to microwave imaging within the contrast source formulation," IEEE Trans. Antennas Propag., vol. 57, no. 4, pp. 1122–1132, Apr. 2009.

[23] H. Harada, D. J. N. Wall, T. Takenaka, and M. Tanaka, "Conjugate gradient method applied to inverse scattering problem," IEEE Trans. Antennas Propag., vol. 43, no. 8, pp. 784–792, Aug. 1995.

[24] S. Tu, J. J. McCombe, D. S. Shumakov, and N. K. Nikolova, "Fast quantitative microwave imaging with resolvent kernel extracted from measurements," Inverse Prob., vol. 31, no. 4, pp. 1–33, Mar. 2015.

[25] D. S. Shumakov, S. Tu, and N. K. Nikolova, "Fast quantitative microwave imaging based on measured point spread functions and inversion in real space," in Proc. IEEE AP-S/URSI Int. Symp. Antennas Propag., Vancouver, BC, Canada, Jul. 2015, pp. 687–688.

[26] P. J. Davis, "Circulant matrices," in Circulant Matrices. New York, NY, USA: Wiley, 1979, pp. 66–189.

[27] C. R. Vogel, "Image deblurring," in Computational Methods for Inverse Problems. Philadelphia, PA, USA: SIAM, 2002, pp. 68–76.

[28] N. K. Nikolova, Introduction to Microwave Imaging. Cambridge, U.K.: Cambridge Univ. Press, 2017.

[29] A. S. Beaverstone, D. S. Shumakov, and N. K. Nikolova, "Frequency-domain integral equations of scattering for complex scalar responses," IEEE Trans. Microw. Theory Techn., vol. 65, no. 4, pp. 1120–1132, Apr. 2017.

[30] D. M. Pozar, "Microwave network analysis," in Microwave Engineering, 2nd ed. Hoboken, NJ, USA: Wiley, 1998, pp. 204–205.

[31] M. S. Zhdanov and S. Fang, "Quasi-linear approximation in 3D EM modeling," Geophysics, vol. 61, no. 3, pp. 646–665, Jun. 1996.

[32] M. S. Zhdanov and E. Tartaras, "Three-dimensional inversion of multitransmitter electromagnetic data based on the localized quasi-linear approximation," Geophys. J. Int., vol. 148, no. 3, pp. 506–519, Mar. 2002.

[33] T. M. Habashy, R. W. Groom, and B. R. Spies, "Beyond the born and Rytov approximations: A nonlinear approach to electromagnetic scattering," J. Geophys. Res., vol. 98, no. B2, pp. 1759–1775, Feb. 1993.

[34] C. Torres-Verdin and T. M. Habashy, "Rapid 2.5-dimensional forward modeling and inversion via a new nonlinear scattering approximation," Radio Sci., vol. 29, no. 4, pp. 1051–1079, Aug. 1994.

[35] B. Chen and J. J. Stamnes, "Validity of diffraction tomography based on the first Born and the first Rytov approximations," Appl. Opt., vol. 37, no. 14, pp. 2996–3006, May 1998.

[36] N. K. Nikolova, "The basics of microwave imaging," in Principles of RF and Microwave Imaging Technology: From Radar to MRI, Short Course SFB," in IEEE MTT-S Int. Microw. Symp. Dig., May 2016, pp. 1–64.

[37] D. S. Shumakov, "Comparison of multi-frequency PSF normalization strategies," McMaster Univ., Hamilton, ON, Canada, Tech Rep. CEM-R-76, Jul. 2016.

[38] *Emerson & Cuming*, Microwave Products Inc., Randolph, MA, USA, Apr. 2013.

[39] D. S. Shumakov, A. S. Beaverstone, and N. K. Nikolova, "De-noising algorithm for enhancing microwave imaging," *IET J. Eng.*, pp. 1–5, Mar. 2017, doi: 10.1049/joe.2016.0207.

[40] M. Slaney, A. C. Kak, and L. E. Larsen, "Limitations of imaging with first-order diffraction tomography," *IEEE Trans. Microw. Theory Techn.*, vol. MTT-32, no. 8, pp. 860–874, Aug. 1984.

[41] R. K. Amineh, M. Ravan, A. Trehan, and N. K. Nikolova, "Near-field microwave imaging based on aperture raster scanning with TEM horn antennas," *IEEE Trans. Antennas Propag.*, vol. 59, no. 3, pp. 928–940, Mar. 2011.

[42] *Taconic CER-10 RF & Microwave Laminate, High DK Material*, Taconic, Petersburgh, NY, USA, Sep. 2013.

[43] *MATLAB R2016a*, MathWorks Inc., Natick, MA, USA, 2016.

[44] M. Redivo-Zaglia and G. Rodriguez, "SMT: A MATLAB toolbox for structured matrices," *Numer. Algorithms*, vol. 59, no. 4, pp. 639–659, Apr. 2012.

[45] K. Khare, *Fourier Optics and Computational Imaging*. Hoboken, NJ, USA: Wiley, 2016, p. 198.

[46] (Mar. 2017). Eric W. Weisstein. *Apodization Function*. From MathWord—A Wolfram Web Resource. [Online]. Available: http://mathworld.wolfram.com/ApodizationFunction.html

Natalia K. Nikolova (S'93–M'97–SM'05–F'11) received the Dipl.Eng. degree from the Technical University of Varna, Varna, Bulgaria, in 1989, and the Ph.D. degree from the University of Electro-Communications, Tokyo, Japan, in 1997.

From 1998 to 1999, she held a Post-Doctoral Fellowship of the Natural Sciences and Engineering Research Council of Canada (NSERC), where she was initially with the Microwave and Electromagnetics Laboratory, DalTech, Dalhousie University, Halifax, NS, Canada, and later, for a year, with the Simulation Optimization Systems Research Laboratory, McMaster University, Hamilton, ON, Canada. In 1999, she joined the Department of Electrical and Computer Engineering, McMaster University, where she is currently a Professor. Her current research interests include inverse scattering and microwave imaging, theoretical and computational electromagnetism, and high-frequency computer-aided design.

Prof. Nikolova was a recipient of the University Faculty Award of NSERC from 2000 to 2005. Since 2008, she has been the Canada Research Chair in High-Frequency Electromagnetics. She is a Fellow of the Canadian Academy of Engineering. She served as a Distinguished Microwave Lecturer from 2010 to 2013. She served as an Associate Editor of the IEEE TRANSACTIONS ON MICROWAVE THEORY AND TECHNIQUES in 2014 and 2015. She currently serves on three IEEE Technical Coordinating Committees: MTT-1 (Computer-Aided Design), MTT-10 (Biological Effects and Medical Applications), and MTT-15 (Microwave Field Theory). She is a correspondent of the International Union of Radio Science.

Denys S. Shumakov (GS'13) received the bachelor's and master's degrees in radio engineering from the National Technical University of Ukraine, Kyiv, Ukraine, in 2008 and 2010, respectively. He is currently pursuing the Ph.D. degree in electrical engineering at McMaster University, Hamilton, ON, Canada.

From 2009 to 2013, he was a Medical Engineer with Materialise NV. He has authored 11 papers and 13 conference proceedings. His current research interests include microwave imaging, inverse scattering, medical imaging, and antenna design.

Mr. Shumakov is a Reviewer for the IEEE TRANSACTIONS ON MICROWAVE THEORY AND TECHNIQUES. He was a recipient of the McMaster International Excellence Award in 2014 and 2015 and the High Field MRI Winter School Scholarship from the Centre for Functional and Metabolic Mapping at the University of Western Ontario, London, ON, Canada, in 2015.